NJC

PAPER

View Article Online
View Journal | View Issue

Cite this: *New J. Chem.*, 2017, **41**, 14351

4-Bis(4-aminophenoxy)phenoxy derivitized phthalocyanine conjugated to metallic nanoparticles: searching for enhanced optical limiting materials†

Njemuwa Nwaji, John Mack and Tebello Nyokong *

Received 25th July 2017,
Accepted 20th October 2017

DOI: 10.1039/c7nj02718d

rsc.li/njc

In this study, the photophysical, nonlinear absorption and nonlinear optical limiting properties of 4-(2,4-bis(4-aminophenoxy)phenoxy) phthalocyinato zinc(II) phthalocyanine (**6**) conjugated to metallic nanoparticles have been investigated using open aperture Z-scan techniques using 532 nm nanosecond pulses. The nonlinear optical response demonstrated that the studied complex and the nanoconjugates exhibit higher excited state absorption cross-section compared to ground state absorption. Enhanced optical limiting performance was observed when complex **6** was conjugated to nanoparticles with **6**CB-AuNPs (CB = covalent bond) showing the highest optical limiting threshold of 0.36 J cm^{-2}.

Introduction

The potential applications of nonlinear optical materials in diverse areas such as in optical information processing, optical computing, harmonic generation, optical switching, and optical limiting (OL)[1] have drawn the attention of researchers towards developing optical materials with enhanced nonlinear optical (NLO) responses. Optical limiters strongly attenuate intense optical beams while exhibiting high transmittance for low-intensity ambient light levels. It has been shown that materials with strong reverse saturable absorption (RSA) can be effectively employed in limiting the output energy of incident light, and hence such materials are of vital interest in optical limiting applications.[2,3]

The NLO and OL properties of phthalocyanines (Pcs) have received considerable attention,[1,3–5] due to their thermal stability and extensive delocalized two-dimensional π-systems. Moreover, the relatively higher ratio of excited state to ground state absorption cross-section and low linear absorption at some wavelengths such as 532 nm make Pcs a potential material of choice for nonlinear applications.

Recent years have witnessed a gradual research focus on OL properties of metallic nanoparticles (NPs) due to their surface plasmon resonance (SPR) bands which can be tuned to enhance their optical properties.[6–8] Conjugates of metallophthalocynines (MPcs) with AuNPs, AgNPs and AuAgNPs have been employed for NLO,[9–11] and AgNPs were found to perform worse than AuNPs since the SPR band for the former is not resonant with 532 nm.[11] The NLO behaviour of nanoparticle-Pcs conjugates depends on the type of link between them. Metal–S[10,11] and amide bonds[9] have been employed. This work reports in detail on the linking of phthalocyanines through possibly both amide and metal–nitrogen bonds (self-assembly), and the NLO behaviour of the resulting conjugate.

The MPc complex employed is 4-(2,4-bis(4-aminophenoxy)-phenoxy)phthalocyinato zinc(II) (**6**) and it is linked to AuNPs and AgNPs. The rotational flexibility of the (4-aminophenoxy) phenoxy substituents is expected to provide polarizability which will enhance the optical limiting properties. The amino groups of complex **6** will be linked to the COOH groups of glutathione (GSH) capped AuNPs and AgNPs through an amide bond. The possibility of metal–nitrogen bonds in addition to amide bonds will also be explored.

Experimental

Materials

Zinc acetate dihydrate, 2,4-dichlorophenol (**1**), 4-nitrophthalonitrile (**2**), 4-aminophenol (**3**), absolute ethanol (EtOH), dicyclohexylcarbodiimide (DCC), 1-pentanol, dimethylaminopyridine (DMAP), 1,8-diazabicyclo[5.4.0] undec-7-ene (DBU), dimethyl sulphoxide (DMSO), DMSO-d_6, and 1, 3-diphenylisobenzofuran (DPBF) were obtained from Sigma Aldrich. Tetrahydrofuran (THF), chloroform, dimethylformamide (DMF), dichloromethane (DCM) and methanol were purchased from SAARCHEM®. Glutathione (GSH) capped

Department of Chemistry, Rhodes University, Grahamstown 6140, South Africa. E-mail: t.nyokong@ru.ac.za; Fax: +27 46 6225109; Tel: +27 46 6038260

† Electronic supplementary information (ESI) available: NMR spectra and MALDI-TOF mass spectra, absorption spectra, EDX spectra, XPS spectra, input *vs.* output plot, biexponential decay curve of complex **6**, and table of theoretical calculations. See DOI: 10.1039/c7nj02718d

AuNPs and AgNPs were synthesized as reported in the literature.[12,13] Oleamine (OA) capped AuNPs and AgNPs were also synthesized as reported in the literature.[14]

Equipment

Infrared spectra were recorded on a Bruker spectrum 100 with the universal attenuated total reflectance (ATR) sampling accessory. ^{1}H NMR spectra were recorded on Bruker® AVANCE II 400 MHz NMR spectrometer using tetramethylsilane (TMS) as an internal reference. Elemental analyses were done using a Vario-Elementar Microcube® ELIII while mass spectral data were collected on a Bruker® AutoFLEX III Smart-beam TOF/TOF mass spectrometer using α-cyano-4-hydrocinnamic acid as the matrix in the positive ion mode. Ground state electronic absorption spectra were recorded on a Shimadzu® UV-2550 spectrophotometer. Fluorescence excitation and emission spectra were measured on a Varian Eclipse® spectrofluorimeter using a 360–1100 nm filter. Fluorescence lifetimes were measured using a time-correlated single photon counting setup (TCSPC) (FluoTime 300, Picoquant® GmbH) with a diode laser (LDH-P-670, Picoquant GmbH, 20 MHz repetition rate, 44 ps pulse width). X-ray diffraction (XRD) patterns were measured on a Bruker® D8 Discover diffractometer, equipped with a Lynx Eye detector, under Cu-Kα radiation (λ = 1.5405 Å). Data were collected in the range from 2θ = 10 to 100°, scanning at 0.010° min^{-1} and 192 s per step. The samples were placed on a zero background silicon wafer slide. Magnetic circular dichroism (MCD) spectra were measured with a Chirascan plus spectrodichrometer equipped with a 1 T (tesla) permanent magnet by using both the parallel and antiparallel fields. The triplet decay kinetics were determined using a laser flash photolysis system. The excitation pulses were produced by a tunable laser system consisting of a Nd:YAG laser (355 nm, 135 mJ/4–6 ns), pumping an optical parametric oscillator (OPO, 30 mJ/3–5 ns). Triplet lifetimes were determined by the exponential fitting of the kinetic curves using the ORIGIN® 8 Professional software. Transmission electron microscope (TEM) images were obtained using a Zeiss 1210 TEM operated at 100 kV accelerating voltage. Energy-dispersive X-ray spectroscopy (EDS) was done on an INCA PENTA FET coupled to the VAGA TESCAM using 20 kV accelerating voltage. Illumination for singlet oxygen and photodegradation quantum yields was performed using a general electric quartz lamp (300 W). A 600 nm glass cut-off filter (Schott®) and water filter were employed to filter off ultra-violet and infrared radiation, respectively. An interference filter, 700 nm with a band of 40 nm, was placed just before the sample chamber. Light intensities were measured with a POWER MAX 5100 (Molelectron® detector incorporated) power meter and were found to be 3.8 × 10^{15} photons cm^{-2} s^{-1} for singlet oxygen and photodegradation studies. X-ray photoelectron spectroscopy (XPS) analysis was done using an AXIS Ultra DLD, with an Al (monochromatic) anode equipped with a charge neutralizer, supplied by Kratos Analytical. The following parameters were used: the emission was 10 mA, the anode (HT) was 15 kV and the operating pressure was below 5 × 10^{-9} Torr. A hybrid lens was used and the resolution to acquire scans was at 160 eV pass energy in slot mode. The centre used for the scans was at 520 eV with a width of 1205 eV, steps at 1 eV and dwell time at 100 ms. The high resolution scans were acquired using 80 eV pass energy in slot mode.

All Z-scan measurements were performed using a frequency-doubled Nd:YAG laser (Quanta-Ray, 1.5 J/10 ns fwhm pulse duration) as the excitation source. The laser was operated in a near Gaussian transverse mode at 532 nm (second harmonic). The liquid samples were placed in a cuvette (internal dimensions: 2 mm × 10 mm × 55 mm, 0.7 mL) with a path length of 2 mm (Starna 21-G-2).

Theoretical calculation

The optimized structures of complex **6** were obtained using the B3LYP functional of the Gaussian 09 software package with 6-31G(d) basis sets.[15] The TD-DFT calculations were carried out using the CAM-B3LYP functional with 6-31G(d) basis sets. The CAM-B3LYP functional contains a long range connection that provides more accurate results for transitions with significant charge transfer character.[16]

Synthesis

Synthesis of 4-(2,4-dichlorophenoxy)phthalonitrile (4). A mixture of 2,4-dichlorophenol (**1**) (1 g, 5.78 mmol) and 4-nitrophthalonitrile (**2**) (0.93 g, 5.78 mmol) was dissolved in 20 mL of DMF and allowed to stir at room temperature under argon gas for 30 min, followed by the addition of K_2CO_3 (1.5 g, 10.85 mmol). The reaction was then allowed to stir at room temperature for a further 48 h. The reaction mixture was poured into ice water and the precipitated product was filtered under reduced pressure and dried under vacuo to give a brownish solid. Yield 1.08 g (56%), IR (ATR): ν (cm^{-1}): 3071 (Ar–C–H stretch), 2968–2839 (Aliph. C–H stretch), 2233 (C–N stretch). ^{1}H NMR (600 MHz, DMSO-d_6) δ 8.20–8.15 (m, 1H, Ar–H), 7.95–7.80 (t, J = 7.64 Hz, 2H, Ar–H), 7.59–7.55 (d, J = 7.52 Hz, 1H, Ar–H), 7.45–7.40 (d, J = 7.58 Hz, 2H, Ar–H). Anal. calc. For ($C_{14}H_6N_2$): C, 58.16; H, 2.09; N, 9.69. Found: C, 58.19: H, 2.08; N, 9.70.

Synthesis of 4-(2,4-bis(4-aminophenoxy)phenoxy)phthalonitrile (5). For the synthesis of **5**, a mixture of **4** (1 g, 3.47 mmol) and 4-aminophenol (**3**) (0.76 g, 6.94 mmol) in dry DMF was heated at 70 °C under argon for 72 h. The reaction mixture was precipitated in ice water, filtered and recrystalized in dry methanol. The resultant yellowish solid was dried under vacuum to yield 0.98 g (55.8%). IR (ATR): ν (cm^{-1}): 3286 (NH_2 stretch), 2928 (Ar–CH), 2232 (C≡N stretch), 1557, 1464 (C=N stretch of primary amine). ^{1}H NMR (600 MHz, DMSO-d6) (δ, ppm): 8.25–8.18 (m, 1H, Ar–H), 8.09–8.05 (d, J = 8.17 Hz, 1H, Ar–H), 7.88–7.83 (d, J = 8.28 Hz, 3H, Ar–H), 7.68–7.64 (m, 3H, Ar–H), 7.52–7.39 (m, 3H, Ar–H), 7.28–7.25 (m, 1H, Ar–H), 6.82–6.76 (d, 1H, J = 7.12 Hz, Ar–H), 6.71–6.68 (d, 1H, J = 6.23 Hz, Ar–H), 5.25 (s, 4H, NH_2 proton) (NMR spectrum in ESI†), anal. calc. for $C_{26}H_{18}N_4O_3$, C, 71.88; H, 4.18; N, 12.90. Found: C, 71.81; H, 4.13; N, 13.02.

Synthesis of tetrakis-4-(2,4-bis(4-aminophenoxy)phenoxy) phthalocyinato zinc(II) (6). A mixture of zinc acetate dihydrate (0.25 g, 1.1 mmol), complex **5** (0.3 g, 0.7 mmol), DBU (0.25 mL)

and 1-pentanol (5 mL) was refluxed at 170 °C for 24 h under argon atmosphere. On cooling, methanol was added and the precipitate was collected through centrifugation. The product was washed with methanol, ethanol and diethyl ether. The dark green product was further purified by column chromatography using THF and methanol (96 : 4) solvent mixture as eluent. The purified product was dried in an enclosed fume hood. Yield: 0.18 g (34%), IR (ATR): ν (cm^{-1}): 3326 (NH_2 stretch), 2928 (Ar–CH), 1595, 1473 (C═N stretch of primary amine). ^{1}H NMR (600 MHz, DMSO-d_6) (δ, ppm): 8.15–8.00 (m, 10H, Ar–H), 7.96–7.80 (m, 13H, Ar–H), 7.65–7.50 (m, 8H, Ar–H), 7.50–7.35 (m, 12H, Ar–H), 7.30–7.15 (m, 3H, Ar–H), 6.92–6.75 (m, 5H, Ar–H), 6.75–6.65 (m, 5H, Ar–H), 5.18 (s, 16H, NH_2 proton). Anal. calc. for $C_{104}H_{72}N_{16}O_{12}Zn$, C, 69.42; H, 4.57; N, 12.11; O, 10.37; Zn, found: C, 69.28; H, 4.62; N, 11.97, UV-vis., λ_{max}/nm (log ε): (DMSO), 681 (5.08), 616 (4.10), 348 (4.50). MALDI TOF-MS: calculated: 1803.21; found: 1802.75.

Attachment of phthalocyanines to nanoparticles by self-assembly (SA)

The surface assembly of the phthalocyanine onto OA capped AuNPs and AgNPs was carried out by refluxing a solution of 5 mg of complex **6** in 10 mL of toulene followed by the addition of 1 mg of the AuNPs or AgNPs in 2 mL of toluene. The reaction was allowed to reflux for 3 h, cooled to room temperature while stirring and subsequently left stirring at room temperature for a further 12 h. The mixture was diluted with methanol and the **6**-nanoconjugates were collected by centrifugation at 5000 rpm for 10 min. The products were washed with methanol and ethanol to remove the unreacted Pcs and are represented as **6**SA-AuNPs and **6**SA-AgNPs (where SA stands for surface assembly).

Covalent linkage of 6 to GSH functionalized AgNPs or AuNPs

The conjugation was performed following a literature method[13] with slight modification. Briefly, 0.005 g of GSH functionalized AgNPs or AuNPs was dissolved in 5 mL of DMF, followed by the addition of DCC (0.017 g, 0.082 mmol) to activate the carboxylic acid functional groups. The reaction mixture was allowed to stir for 48 h at ambient temperature. After this time, DMAP (0.010 g, 0.082 mmol) and complex **6** (0.040 g, 0.02 mmol) were added and the mixture was allowed to stir for a further 48 h at ambient temperature. The formed nanoconjugates were precipitated out of solution with methanol and collected through centrifugation, washed several times using ethanol and dried in an enclosed fume hood. The products are represented as **6**CB-AuNPs and **6**CB-AgNPs (where CB stands for covalent bonding).

Photophysicochemical properties

Fluorescence and triplet quantum yields. The fluorescence (Φ_F) and triplet (Φ_T) quantum yields were determined using the comparative methods according to literature reports,[17–19] using ZnPc as a standard (Φ_F = 0.20)[19] and (Φ_T = 0.65)[18] in DMSO.

Singlet quantum yield (Φ_Δ) and photodegradation (Φ_{Pd}) quantum yields. A comparative chemical method was employed to evaluate the singlet quantum yield (Φ_Δ) of complex **6** and its corresponding nanoconjugates using ZnPc as a standard in DMSO (Φ_Δ = 0.67)[18] and DPBF as a chemical quencher for singlet oxygen in DMSO. The concentrations of DPBF were lowered to 0.3 μmol dm^{-3} for all the solutions, to avoid chain reactions and its degradation was monitored at ~417 nm.

The photodegradation quantum yield (Φ_{Pd}) was determined using eqn (1)[18]

$$\Phi_{Pd} = \frac{(C_0 - C_t)V_R}{I_{abs} \cdot t} \quad (1)$$

where C_0 and C_t in mol dm^{-3} are the concentrations of the sample prior to and after irradiation, respectively; V_R is the solution volume; t is the irradiation time per cycle and I_{abs} is defined by eqn (2).

$$I_{abs} = \frac{\alpha A I}{N_A} \quad (2)$$

where α = 1–$10^{-A(\lambda)}$ ($A(\lambda)$ is the absorbance of the sensitizer at the irradiation wavelength), A is the irradiated area (2.5 cm^2), I is the intensity of light (3.8×10^{15} photons cm^{-2} s^{-1}) and N_A is Avogadro's constant.

Results and discussion

Synthesis and characterization of complex 6

The synthetic route of complex **6** is depicted in Scheme 1. 2,4-Dichlorophenol (**1**) was reacted with 4-nitrophthalonitrile (**2**)

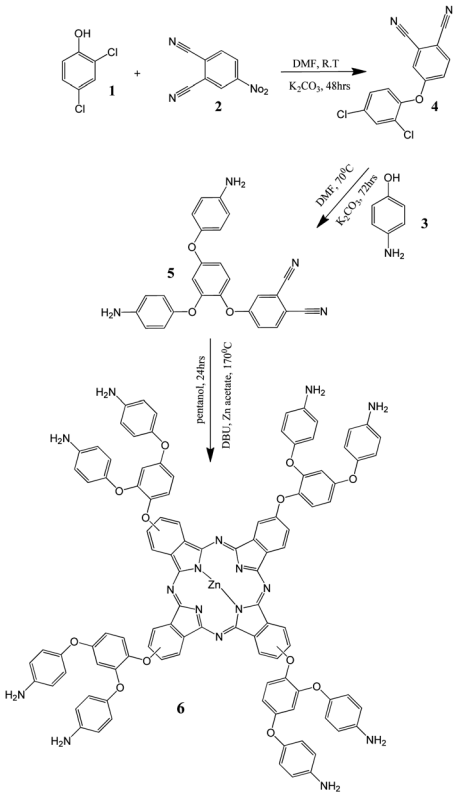

Scheme 1 Synthetic route for 4-(2,4-bis(4-aminophenoxy)phenoxyl)-phthalocyinato zinc(II) (**6**).

to yield 4-(2,4-dichlorophenoxy)phthalonitrile (**4**), which was subsequently reacted to 4-aminophenol (**3**) to give the precursor 4-(2,4-bis(4-aminophenoxy)phenoxy)phthalonitrile (**5**). Cyclotetramerization of the phthalonitrile (**5**) using 1-pentanol as a solvent and a catalytic amount of DBU gave complex **6**. The disappearance of the CN peak at 2232 cm^{-1} (for **5**) in the FT-IR spectrum of **6** confirmed the formation of the latter. The ^{1}H NMR spectra for **6** showed aromatic ring protons between 8.15 and 6.65 ppm, whereas the amino protons were confirmed at 5.18 ppm integrated into 16 protons (the ^{1}H NMR spectra are provided as ESI,† Fig. S1). The existence of multiple heavy isotopes with an increase in the mass of a molecule causes a decrease in the relative abundance of the monoisotopic peak; hence the isotopic distribution model has been shown to be the accurate method of assigning molecular mass in large molecules.[20] The isotopic mass distribution of complex **6** was simulated and compared with the experimental MALDI-TOF measured masses. The observed mass of the complex is in agreement with the calculated value (Fig. S2, ESI†). The elemental analysis also confirmed the structure of complex **6** shown in Scheme 1.

Electronic absorption studies

The ground state absorption spectrum for **6** contains two absorption peaks, at 348 nm and 680 nm. These bands can readily be assigned to the B and Q transitions, respectively, in accordance with Gouterman's 4-orbital model[21] on the basis of the MCD spectroscopy and TD-DFT calculations (Fig. 1). The observed and calculated spectral properties are consistent with what is normally anticipated for a monomeric metal phthalocyanine complex.[22] MCD spectroscopy is a specialist complementary technique that provides information on ground and excited state degeneracies, which is essential in understanding the electronic structure of metal complexes of high symmetry.[22] Although the MCD signal arises from the same transition that is responsible for the corresponding bands in the UV-visible absorption spectrum, the selection rules for the two techniques are different due to the use of circularly polarized light and an applied magnetic field in the context of MCD spectroscopy.

The MCD spectrum of **6** contains a distinctive S-shaped sigmoid curve between 600 and 690 nm with a cross-over point of 681 nm, which almost exactly corresponds to the 680 nm absorption maxima (Fig. 1). It can therefore be assumed that the MCD spectrum in this spectral region is dominated by a pseudo-A_1 term and hence the transition involves a near degenerate excited state.[22] A similar curve is also observed in the MCD spectrum at *ca.* 345 nm. From the MCD spectroscopy, we can readily assign the 680 and 348 nm bands to the Q and B transitions, respectively, in accordance with Gouterman's four-orbital model,[21] since these bands are expected to give rise to the most intense MCD bands as they are associated with orbital angular momentum changes on the core of the macrocycle.[21] Gouterman's 4-orbital model has been modified in the context of phthalocyanines to include two close-lying B_1 and B_2 bands, due to the effect of configurational interaction with other higher energy ππ* states.[22] The broad shoulder of absorbance to the red of the main B_1/B_2 band envelope that gives rise to relatively weak bands in the MCD spectrum can be attributed to the bands that are predicted to lie to the red of the B_1 and B_2 bands in the TD-DFT calculation (Fig. 1 and Table S1, ESI†).

Similar absorbances have been reported previously for Pcs with alkoxy, phenoxy, thioalkyl and thiaaryl substituents and have been attributed either to n → π* transitions that are associated with the lone pairs on peripheral oxygen or sulphur atoms, or to π → π* transitions that are associated with low-lying occupied π-MOs (MO = molecular orbital) that are localized largely on the peripheral benzene rings, which are destabilized by the electron donating substituents.[23]

Fig. 2 shows the emission and excitation spectra of complex **6** in DMSO. It can be seen that the excitation spectra are similar to the absorption spectra and both are mirror images of the emission spectra. The proximity of the Q-band of absorption to that of the excitation maxima indicates that the nuclear configurations of the ground and excited states are similar and were not affected by excitation in DMSO.

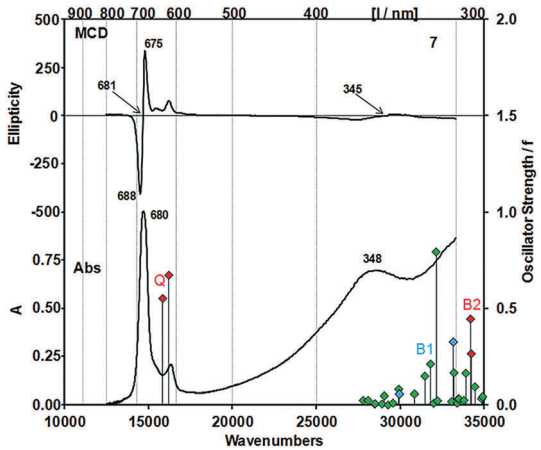

Fig. 1 Absorption and MCD spectra of **6** in DMSO. The calculated TD-DFT spectrum of the D_{4h} isomer of **6**. Red diamonds are used to highlight bands associated with the main Q and B bands of Gouterman's 4-orbital model[21] that are associated with transition out of the $1a_{1u}$ and $1a_{2u}$ MOs into the 1eg* LUMO while the blue diamonds are used for the B_2 band[22] that is associated primarily with a transition out of the $2a_{2u}$ MO. Details of the calculations are provided in Table S1, ESI.†

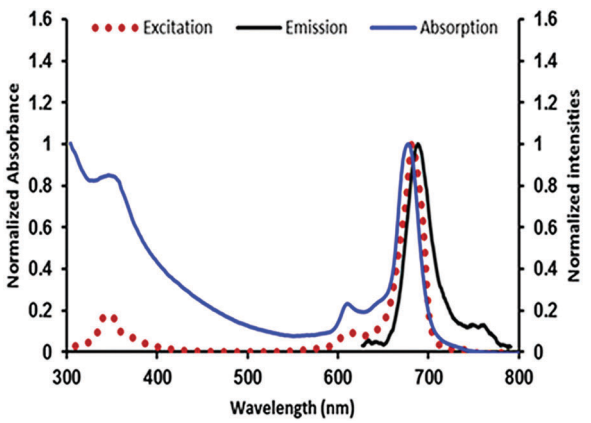

Fig. 2 Absorption, excitation and fluorescence spectra of **6** in DMSO.

Synthesis and characterization of the nanoconjugates

Scheme 2 shows the pathway for the surface assembly as well as covalent linkage of complex **6** to the metallic nanoparticles. The ligand exchange was used for the attachment of the phthalocyanines onto the surface of the nanoparticles, where the loosely bound oleyamine ligands were partially replaced by Pcs that bind to the surface of the nanoparticles.[24] The nitrogen on the peripheral aminophenoxy substituents was used to attach the phthalocyanine complexes onto the AuNP and AgNP surfaces due to the affinity of gold and silver for nitrogen atoms.

For covalent linkage, the NH_2 in complex **6** was coupled with the COOH group of the gluthathione functionalized nanoparticles to form an amide bond using DCC and DMAP as activating and coupling agents, respectively. Considering the approximate size of Pc (1 nm), which is far less than that of the nanoparticles (>5 nm), it is possible that more than one Pc is linked to the nanoparticles. The loading of complex **6** onto the nanoparticles was investigated following literature methods.[25] This involves investigating the ratio of metallic nanoparticles required to saturate the dyes molecule, hence resulting in complete disappearance of the Q-band (Fig. S3, ESI†). The concentration of complex **6** was kept constant throughout the experiment. A decrease in the absorption band of **6** was observed as the ratio of the nanoparticles loaded increases. The absorption band of **6** completely disappears at a [Au]/[complex **6**] ratio of 6.4 (Fig. S3, using GSH-AuNPs and OA-AgNPs as examples, ESI†). The number of gold atoms per particle (NAu) was determined from the expression NAu = $(59\ \mathrm{nm}^{-3})(\pi/6)(D_{MS})^3$ [26] where D_{MS} is the mean diameter of the particles as found from TEM. Thus, for a gold nanoparticle with 11.28 nm, the number of gold atoms is calculated to be 44 356. Using the ratio [Au]/[complex **6**] of 6.4, the number of complex **6** molecules per gold nanoparticle was determined to be 6930. With known molecular weight of **6**, the mass of complex **6** per unit area of nanoparticles was calculated

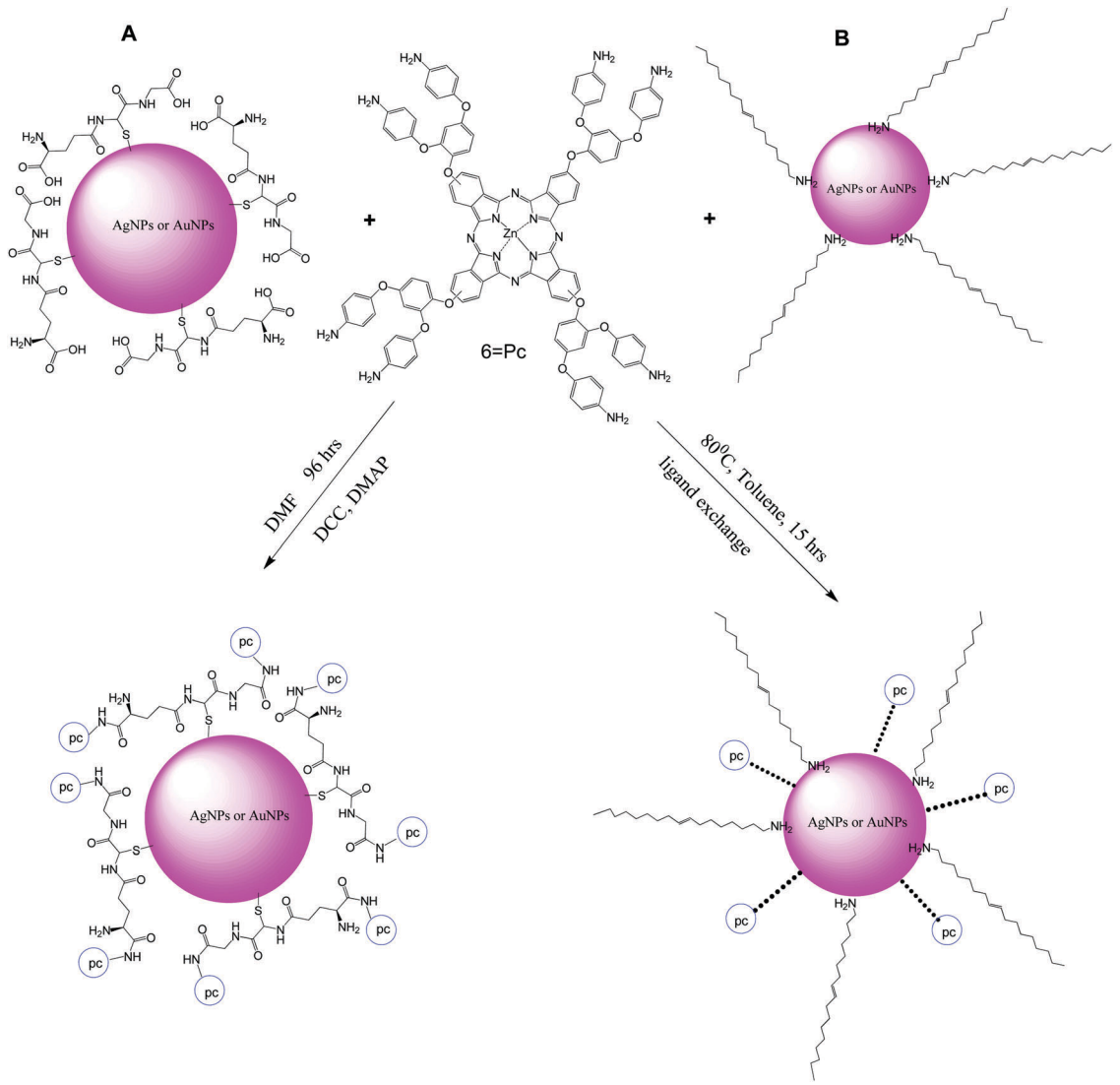

Scheme 2 Illustration of the synthetic route for conjugation of complex **6** to GSH functionalized (route A) and oleyamine stabilized (route B) silver and gold nanoparticles.

Table 1 Photophysicochemical parameters of complex **6** and its conjugates, in DMSO. Excitation for emission at 620 nm and excitation for the triplet at 675 nm

Conjugate[a]	Size[b] (nm) (TEM)	Size[b] (nm) (XRD)	Pc loading (g pc per cm^2 NPs)	SPR band (nm)	Φ_F	τ_f (ns)	Φ_T	τ_T (μs)	τ_{isc} (ns)	k (s^{-1}) (10^4)	Φ_Δ	Φ_{pd} 10^{-6}
6	—	—	—	680 (Q band)	0.21	3.25	0.61	343	5.33	5.71	0.37	2.09
6SA-AuNPs (OA-AuNPs)	11.28 (10.50)	11.81 (10.98)	28	528 (523)	0.13	2.64	0.66	312	3.94	4.83	0.44	1.58
6SA-AgNPs (OA-AgNPs)	12.05 (9.02)	13.17 (9.84)	16	423 (410)	0.15	3.12	0.63	325	4.95	5.04	0.40	1.52
6CB-AuNPs (GSH-AuNPs)	11.61 (12.30)	12.03 (13.41)	30	529 (529)	0.09	2.05	0.75	298	2.73	3.97	0.53	1.03
6CB-AgNPs (GSH-AgNPs)	14.27 (10.50)	13.02 (10.29)	37	473 (400)	0.10	3.02	0.68	303	4.44	4.21	0.47	1.25

[a] Starting NPs in brackets. [b] Values in brackets are for NPs alone.

and presented in Table 1. For the surface assembly of **6**, it was found that the number of Pcs loaded onto the AgNPs is greater than the number loaded onto AuNPs. This could be attributed to the smaller size of the AgNPs with higher surface to volume ratio compared to AuNPs (to be discussed below, see also Table 1). The number of Pcs loaded through the covalent route was found to be higher than the number loaded through surface assembly. This could be explained using the fact that complex **6** as well as the oleyamine used to stabilize the nanoparticles both possess amine groups; therefore ligand exchange will tend to be slow, while there are more Pcs loaded through the covalent route since the activated COOH from the glutathione functionalized nanoparticles will be more prone to attack by the amino group of complex **6** through amide linkage. Another possibility of low loading through the surface assembly route could arise from the steric hindrance from the oleyamine capping agent. The OA capped AuNPs and AgNPs exhibit their surface plasmon resonance (SPR) of AuNPs at 523 nm and 410 nm respectively (Fig. 3, Table 1 and Fig. S4, in ESI†). The SPR peaks shifted to 529 nm for GSH capped AuNPs and to 400 nm for GSH capped AgNPs, Table 1. Upon conjugation of complex **6** to the nanoparticles (Fig. 3, **6**CB-Ag NPs and **6**SA-AuNPs as examples and Table 1), the surface plasmon resonance bands slightly shifted from 523 nm for OA-AuNPs to 528 nm for **6**SA-AuNPs (Fig. 3B), while **6**SA-AgNPs showed significant red shifting of the SPR band at 423 nm from 410 nm for OA-AgNPs (Fig. S4, ESI† and Table 1). For the covalent conjugates, there is no shift in the SPR band for **6**CB-AuNPs compared to GSH-AuNPs, but there is a huge red shift for **6**CB-AgNPs (473 nm) compared to GSH-AgNPs (400 nm), Table 1.

The red shifting in the SPR band is associated with aggregation and increase in size of the nanoparticles.[27] For all the conjugates (except for **6**CB-AuNPs), there is an increase in size on conjugation to complex **6** (to be discussed below), hence there is red shifting in the SPR band. No red shifting is observed in the SPR band for **6**CB-AuNPs, since there was no increase in size as will be discussed below.

It is pertinent to note that the Q-band of complex **6** maintains its original 680 nm absorption band after conjugation in both the surface assembled and the covalently linked derivatives. The observed presence of the SPR band in the conjugates indicates successful conjugation of the nanoparticles to complex **6**.

Fig. 4 shows the FT-IR spectra upon covalent linkage of complex **6** to GSH functionalized nanoparticles (**6**, **6**CB-AuNPs and GSH-AuNPs as examples). The two stretches from the primary amine of complex **6** alone were observed at 1492 cm^{-1} and 1594 cm^{-1}. Upon covalent linkage of **6** to the nanoparticles, a distinct and sharp single vibration band was observed for **6**CB-AuNPs at 1649 cm^{-2} and 1638 cm^{-2} for **6**CB-AgNPs indicating conversion of primary amine to secondary amine with the formation of an amide bond (O═C–NH). This confirms the successful formation of the amide bond between the Pc and the NPs because this band was not present in either of the two individual components. Also, the increased intensity and

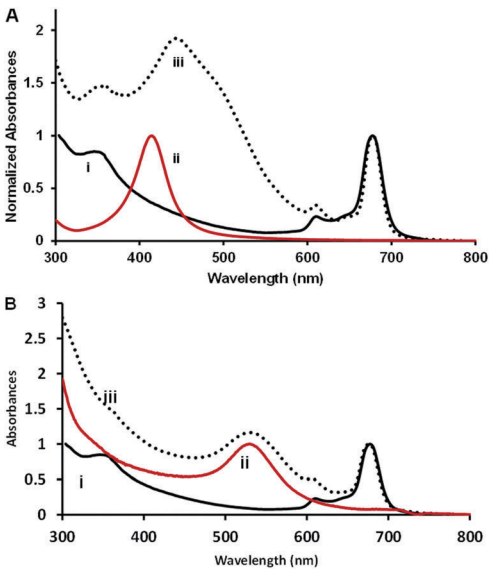

Fig. 3 Absorption spectra of (A) **6** (i), GSH-AgNPs (ii) and **6**CB-AgNPs (iii), and (B), **6** (i), OA-AuNPs (ii) and **6**SA-AuNPs (iii) in DMSO.

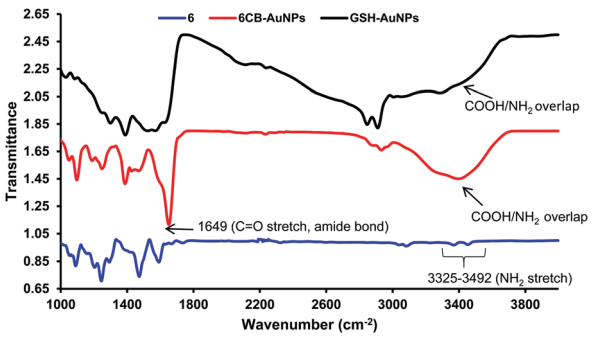

Fig. 4 FTIR spectra of **6** and its covalently linked AuNPs.

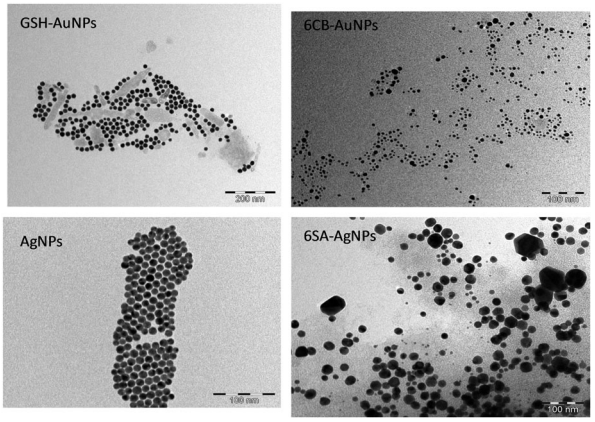

Fig. 5 Representative TEM images of nanoparticles alone and when conjugated to complex **6**.

broadening between 3432 and 3500 cm^{-1} in the nanoconjugate indicate overlap of the NH_2 and COOH stretches and from the Pc and the GSH functionalized nanoparticles.

The TEM micrographs of the GSH-AuNPs and OA-AgNPs (as examples) are consistent with monodispersed particles. The average sizes for OA-AuNPs and OA-AgNPs were determined to be 10.50 nm and 9.02 nm respectively (Fig. 5 and Table 1) and upon functionalization with glutathione, the average sizes were found to be 12.30 nm and 10.50 nm for GSH-AuNPs and GSH-AgNPs, respectively. Thus, the AgNPs were smaller than the AuNPs. Upon conjugation, there was an increase in size for all except for **6**CB-AuNPs where there was a decrease in size.

Increase in the size of nanoparticles after conjugation to a chromophore is a well-known phenomenon,[27,28] due to the formation of aggregates as well as π–π interactions between the Pcs and nanoparticles following conjugation. The increase in the size of the nanoconjugates can be attributed to interactions between the MPcs on adjacent NPs *via* π–π stacking.

The surface curvature and damping of electrons in metallic nanoparticles can affect the shifts of the SPR band.[29,30] With a very low surface curvature (large particle size) the surface plasmon can become stiffer because the orbitals overlap to a greater degree, which will lead to a high energy resonance, and hence lower SPR wavelength (blue shift). With a high surface curvature (small particle size) the surface plasmon becomes more loose because the orbitals are slightly farther apart, resulting in a lower-energy resonance (and therefore the observed red-shift for smaller particles). Thomas *et al.*[29] employed a classical model to predict that damping of electron motion results in red-shift of SPR of silver nanoparticles when the size was reduced from 10 nm to 5 nm. The reverse case of blue shifting of the SPR peak with increase in particle size was observed by Fleger and Rosenbluh[30] in gold-silver nano-alloys. This applies only when comparing OA-AgNPs and GSH-AgNPs, but not for the conjugates.

The interfacial interaction such as adsorption of the ligand can affect the surface curvature of metallic nanoparticles[31] depending on orientation. Thus, the observed decrease in size in **6**CB-AuNPs could be attributed to orientative change in surface curvature or damping of electrons within the particle matrix due to adsorption of complex **6**.

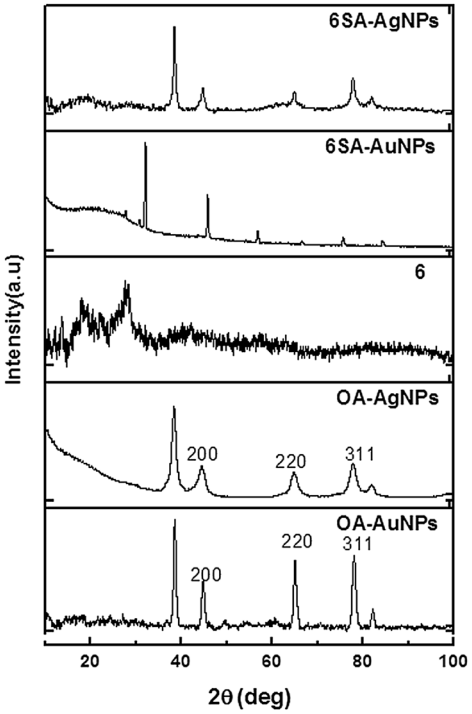

Fig. 6 Representative XRD diffractograms of complex **6** and the corresponding nanoconjugates.

The elemental compositions of the nanoparticles and conjugates were qualitatively determined using energy-dispersive X-ray spectroscopy (EDX), Fig. S5 (ESI†). The EDX of the NPs alone showed the expected atoms. On conjugation of **6** to AgNPs or AuNPs (**6**SA-AgNPs and **6**CB-AuNPs as representatives), additional peaks (Zn) were observed indicating the presence of the Pc in the nanoparticles.

The X-ray powder diffraction patterns of the AuNPs and AgNPs alone and upon conjugation to **6** are shown in Fig. 6 (for AuNPs, AgNPs, **6**, **6**SA-AuNPs and **6**SA-AgNPs as examples). The XRD diffraction patterns of the nanoparticles showed well-defined crystalline peaks assigned to the 111, 200, 220, 311 and 222 planes, corresponding to the face-centred cubic structures of metallic gold and silver.[32] The XRD pattern of **6** contains a broad peak between 2θ = 17 and 25°, which is consistent with the amorphous nature of phthalocyanines.[33] Upon conjugation to form nanoconjugates, slight broadening was observed, along with an additional peak near 22°, which provides evidence for the presence of phthalocyanine.

The NP sizes from XRD were calculated using the Debye–Scherrer equation, eqn (3)[34]

$$d = \frac{k\lambda}{\beta \cos\theta} \quad (3)$$

where λ is the wavelength of the X-ray source (λ = 1.5405 Å), k is an empirical constant equal to 0.9, β is the full width at half maximum of the diffraction peak and θ is the angular position. The sizes were obtained by focusing on the (111) peak of

the nanoparticles. The sizes were found to be between 9.84 and 13.41 nm for the nanoparticles alone while for the nanoconjugates, the sizes were observed between 11.81 and 13.17 nm, which are in close agreement with the TEM values (Table 1). Again, there is an increase in the sizes upon conjugation with the exception of **6**CB-AuNPs.

X-ray photoelectron spectroscopy (XPS) is a highly sensitive diagnostic method for the assessment of the chemical state of elements. The interaction of complex **6** with the metallic nanoparticles was investigated using XPS.

XPS high resolution analysis (Fig. 7) was employed to prove the possible interactions of the amino groups of complex **6** with the surface of the nanoparticles as well as the formation of an amide bond upon covalent linkage of **6** to the glutathione functionalized nanoparticles. The XPS N1s spectrum of complex **6** alone gives peaks at 396.1 eV (N–C) and 397.5 eV (N–H). Upon surface assembly of **6** onto gold nanoparticles to form **6**SA-AuNPs, two sets of N1s doublets were observed, one centred around 397.7 eV and the other at 400.8 eV (Fig. 7). The corresponding silver nanoconjugate also showed a similar trend with binding energy at 397.3 eV and 399.7 eV (Fig. S6, ESI†). The presence of two sets of doublets following surface assembly indicates the existence of the amino nitrogens N1s in two different environments. The most logical conclusion in this case would be that some amino 'arms' of complex **6** underwent N–Au or N–Ag interaction following surface assembly while others did not. The set of doublets was resolved using peak fitting in order to investigate different nitrogen groups present. The peak at 400.8 eV is assigned as nitrogen bound to gold, while the peak at 397.7 eV could indicate unbound nitrogen. The presence of bound nitrogen is proof of binding of complex **6** with the nanoparticles. Xiao *et al.*[35] reported a binding energy of 399.2 eV for unbound amino nitrogen and 401.7 eV for hydrogen bound amines, while Zhang *et al.*[36] also observed a binding energy of 398.8 eV and 401.5 eV for free amine and amine bound to gold nanoparticles, respectively.

Fig. 7 also shows the high resolution XPS spectra for **6**CB-AuNPs (**6**CB-AgNPs shown in Fig. S6 (ESI†)). GSH-AuNPs alone showed binding energy for the N–C peak at 396.3 eV, N–H at 397.8 eV and N–C═O at 400.2 eV (Fig. 7). The GSH-AgNPs alone showed a similar trend with binding energy for the N–C peak at 396.7 eV, N–H at 397.3 eV and N–C═O at 400.2 eV (figure not shown). After covalent linkage of **6** to the nanoparticles (for **6**CB-AuNPs), similar peaks were observed but with significant increase in intensity from 132 cps in GSH-AuNPs to 1520 cps in **6**CB-AuNPs as well as shift in the peak due to the amide bond (N–C═O) to 399.6 eV from 400.2 eV for GSH-AuNPs alone. A similar trend was also observed for **6**CB-AgNPs with shift in the amide bond to 399.5 eV (Fig. S6, ESI†). The increase in intensity could be attributed to the conversion of COOH of the glutathione functionalized nanoparticles to an amide bond *via* the interaction with the amino group of **6**. This conversion of the COOH to an amide will lower the electron polarizability of the carboxyl group in the covalently linked nanoconjugates, which informs the shift in binding energies due to electron distortion.

Photophysicochemical studies

Fluorescence quantum yields and lifetimes. The fluorescence quantum yields for **6** and the nanoconjugates range from 0.09 to 0.21 (Table 1) with complex **6** having the highest quantum yield. A significant decrease in fluorescence quantum yield was observed upon conjugation of complex **6** to nanoparticles, due to the heavy atom effect of the latter, which promotes intersystem crossing to the triplet state. The covalently linked nanoconjugates showed lower fluorescence quantum yield than the corresponding surface assembled analogue, probably due to the higher number of Pcs loaded through the covalent route. The higher number of Pcs could lead to aggregation, resulting in quenching of fluorescence.

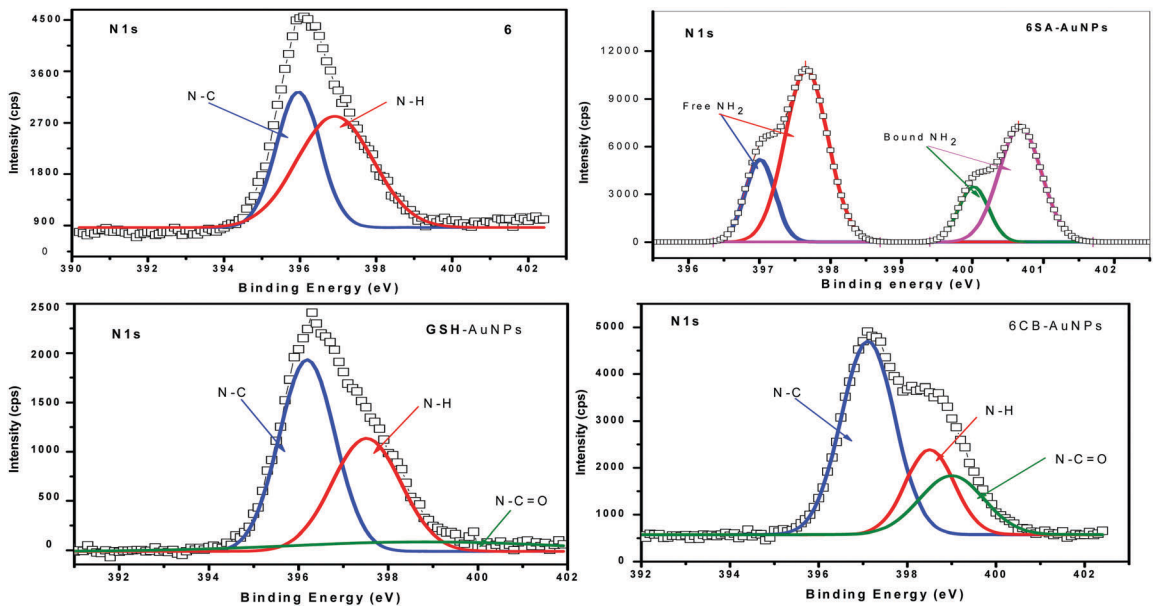

Fig. 7 High resolution XPS N 1s spectra for **6**, GSH-AuNPs, **6**SA-AuNPs and **6**CB-AuNPs.

The fluorescence lifetime decay curve for complex **6** (Fig. S7, ESI†) showed a monoexponential decay curve with a singlet excited lifetime of 3.25 ns. Bi–exponential lifetimes were observed for the conjugates. The presence of two lifetimes upon conjugation of Pcs to nanoparticles could be due to different orientations of the Pcs. The average lifetimes of the nanoconjugates were calculated and presented in Table 1. The decrease in lifetime for the nanoconjugates corresponds to a decrease in fluorescence quantum yield since both have a direct relationship.

Triplet quantum yield and lifetime

One prerequisite property for an ideal optical limiting material is possession of a low fluorescence quantum yield and lifetime, with a corresponding high triplet state quantum yield. A typical triplet decay curve is shown in Fig. S8 (ESI†), using **6**CB-AuNPs as an example. The triplet absorption data were fitted to rate eqn (4) in order to determine the triplet lifetime (τ_T)

$$A_t = A_0 e^{\left(-\frac{t}{\tau_T}\right)} + kt \quad (4)$$

where $A(t)$ and A_0 are the relative absorbance at time $t = t$ and $t = 0$ respectively, k is the triplet state absorption rate constant and τ_T is the triplet excited lifetime. A best fit to eqn (4) showed triplet lifetimes ranging from 298 μs to 343 μs (Table 1). The corresponding triplet quantum yield values range from 0.61 to 0.75 (Table 1). The triplet lifetimes are longer when the triplet quantum yields are smaller as expected. Triplet quantum yields increase for **6** in the presence of the nanoparticles due to the heavy atom effect of the latter.

The corresponding rate constants (k) for the triplet absorption were found to range from 3.97×10^4 s^{-1} to 5.71×10^4 s^{-1} (Table 1), which shows that at every point in time within the irradiation period, 3.97×10^4 to 5.71×10^4 of the complexes are available in the T_1 state (Fig. 8). This could only be valid with the assumption that:

1. All transitions to excited states occur from the ground state, S_0.

2. The population of the S_1 state is confined by the rate of its deactivation to S_0 or its conversion to the T_1 state through intersystem crossing.

3. The population of S_n states is negligible ($S_n \approx 0$) since the time-scale of S_n is shorter than the nanosecond pulse duration of the laser.

4. The intersystem crossing transition from S_1–T_1 becomes spontaneous only when the population of S_1 has been saturated.

5. The S_1–T_1 transition is determined by the quantum mechanical condition, $\Delta N = N_t$, where N_t is the number density of excited molecules in the T_1 state per unit time.

Based on these assumptions, **6**CB-AuNPs with $\Delta N = 3.97 \times 10^4$ will show faster transitions from T_1–T_n than the rest of the complexes, which could account for an enhancement of the triplet–triplet absorption transition in the former.[37]

The intersystem crossing lifetimes were calculated using the relationship (τ_F/Φ_T) where τ_F and Φ_T are fluorescence lifetime and triplet quantum yield, respectively. A faster rate of intersystem crossing results in enhanced nonlinear optical properties and a shorter intersystem crossing lifetime.

The intersystem crossing lifetimes of the complexes showed that **6**CB-AuNPs have the lowest value of 2.73 ns while **6** has the longest value of 5.33 ns. Therefore, **6**CB-AuNPs are expected to show enhanced NLO properties as will be discussed later.

Singlet oxygen (Φ_Δ) and photodegradation (Φ_{pd}) quantum yields

Efficient interaction of the triplet state of a photosensitizer with ground state molecular oxygen can result in the generation of singlet oxygen due to energy transfer from the photosensitizer to the molecular oxygen. In order to determine the singlet oxygen quantum yield (Φ_Δ), the chemical photodegradation of a singlet oxygen quencher (DPBF) was monitored over a period of time (Fig. 9, as an example for complex **6**). The Q-band of the complex did not decrease during irradiation showing stability over the irradiation period, while DPBF degraded. A significant increase in singlet oxygen generation as evidenced by singlet oxygen quantum yield (Table 1) was observed upon conjugation of complex **6** to the metallic nanoparticles corresponding to increase in triplet quantum yields.

Photodegradation is the measure of stability of molecules upon irradiation and it is especially important for molecules that are intended for use in nonlinear optical studies. Photostable

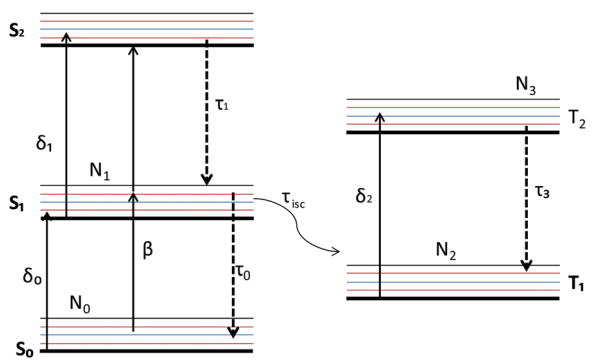

Fig. 8 Five-level energy diagram explaining the dynamics of the excited state population (solid arrows), and non-radiative relaxation (dashed arrows) in the studied complexes.

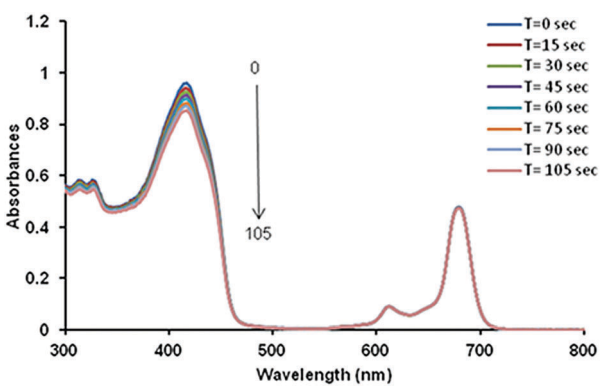

Fig. 9 Typical spectra observed during the generation of singlet oxygen using DPBF as a singlet oxygen quencher for complex **6** in DMSO.

molecules will give better nonlinear optical response since they can absorb intense laser radiation over a long period. The higher the photodegradation quantum yield value, the lower the photostability of the molecule. A good correlation is expected between the photodegradation quantum yield and singlet oxygen production since singlet oxygen has been implicated in phthalocyanine photodegradation, though not in all cases.[38] The nanoconjugates were more photostable compared to complex **6** alone with **6**CB-AuNPs showing the highest photostability which is expected to improve the nonlinear optical response.

Nonlinear optical (NLO) studies

The enhanced nonlinear optical response of Pcs when conjugated to nanoparticles has been reported.[9–11] On the other hand, the possession of surface plasmon resonance (SPR) by the metallic nanoparticles such as AuNPs and AgNPs gives rise to absorption due to the oscillation of free electrons from the conduction band of the metals. Modification of the surface geometry of the metallic NPs leads to a shift in the electric field density on the surface[39] resulting in nonlinear optical response.

The nonlinear response of complex **6** and the corresponding nanoconjugates was measured by using the open aperture Z-scan technique with excitation pulses of 10 ns at a wavelength of 532 nm and a peak intensity of 360.0 MW cm^{-2}. Possession of a reverse saturable absorption (RSA) Z-scan profile is one prominent feature of a nonlinear absorber that is suitable for optical limiting applications.[40,41] The Z-scan profiles of complex **6** and the nanoconjugates showed RSA profiles around the focus (Fig. 10), indicating a good optical limiting potential of the complexes.

The mechanism for RSA in Pcs has been described in the literature using the five-level energy model (Fig. 8). It is also well established that at 532 nm in the nanosecond regime, the observed nonlinear absorption response of phthalocyanines and related macrocycles is dominated by excited state absorption from the singlet and/or triplet excited states rather than two-photon absorption.[42,43] Therefore, accurate knowledge of excited state lifetimes is vital to pin-point the exact contribution of each state to the nonlinear optical response of the material. A five-level energy model[41–44] has been known to account for transitions from $S_1 \rightarrow T_1$, $T_1 \rightarrow T_n$ as well as the two-photon absorption process in the nanosecond time scale.[43] The triplet state population will depend on the intersystem crossing rate and the triplet lifetime.

The τ_{isc} values for complexes **6** and the conjugates ranged from 2.73 to 5.33 ns while the triplet lifetime ranges from 298 to 343 μs (Table 1). Since the triplet lifetime is longer than the intersystem crossing lifetime, there will be more crossovers through intersystem crossing to populate the triplet state. Subsequent absorption of laser radiation will result in further excitation of molecules from the T_1 state to a higher energy T_n state with an excited state absorption cross section, δ_2. The five-level systems in Fig. 8 can be treated with 5-level model rate eqn (S1)–(S7), (ESI†).

Since the lifetimes of the S_n and T_n states are very short when compared to a nanosecond time,[45,46] these levels can be neglected, and only the time variation of populations N_0, N_1 and N_2 for the S_0, S_1 and T_1 energy levels is included in eqn (S1)–(S4) (ESI†). The rate equations were numerically solved following the methods by Zhang *et al.*[45] Fig. 10 shows the experimental data (scattered points) and theoretical fit (solid lines) for complex **6** and upon conjugation to nanoparticles. The ground state absorption cross-section was obtained from absorption spectroscopy using eqn (5)

$$\delta_0 = \frac{\alpha}{N_0} \tag{5}$$

where α is the linear absorption and N_0 is the number of molecules per cm^3.

The five-level model rate equation fitting of the experimental data showed a downward dipping z-scan profile indicating a reverse saturable absorption behaviour with a decrease in transmittance at the focal position ($z = 0$) resulting from excited state induced positive nonlinear absorption of the incident light. Upon conjugation of complex **6** to metallic nanoparticles, the RSA dip increases further, indicating enhanced nonlinear response for the nanocojugates.

The covalently linked nanoconjugates showed more nonlinear optical response with minimum transmittance values of 62% and 53% for **6**CB-AuNPs and **6**CB-AgNPs compared with 46% and 37% (Fig. 10) for the corresponding surface assembled **6**SA-AuNPs and **6**SA-AgNPs, respectively, which could be attributed to more Pcs being loaded on the surface of the nanoparticles through the covalent route compared with the surface assembled route. The RSA in phthalocyanines in the nanosecond regime is dependent on the absorption cross-section of the excited singlet as well as the triplet manifold compared with the ground state. Generally, a good optical limiting (OL)

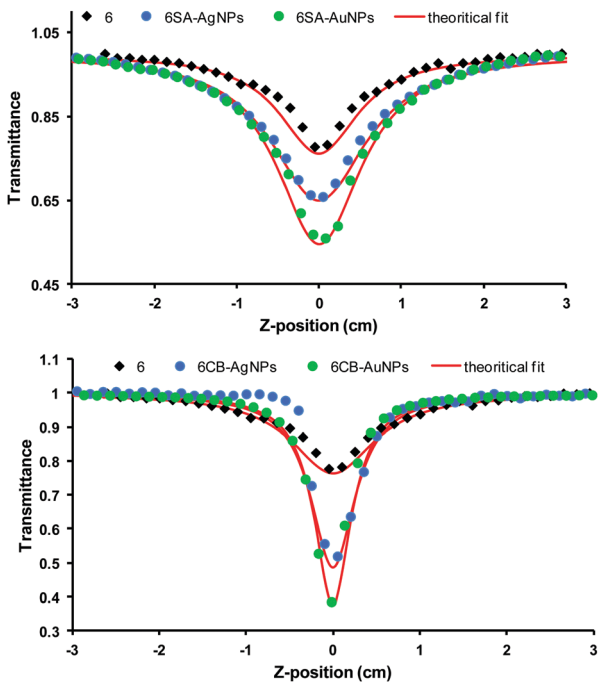

Fig. 10 Open aperture Z-scan of complex **6** and its nanoconjugates in DMSO.

Table 2 Nonlinear optical properties of complex **6** and its nanoconjugates in DMSO

Complex	δ_{TPA} (cm^4 s per photon)	δ_0 (cm^2) 10^{-17}	δ_1 (cm^2) 10^{-16}	δ_2 (cm^2) 10^{-16}	δ_1/δ_0	δ_2/δ_0	I_{lim}
6	2.16×10^{-46}	2.97	2.02	3.97	6.8	13.4	0.87
6SA-AgNPs	1.36×10^{-48}	1.78	3.37	5.30	6.6	10.3	0.75
6SA-AuNPs	3.91×10^{-45}	2.05	4.47	4.40	21.8	21.5	0.68
6CB-AgNPs	2.86×10^{-46}	2.27	3.15	4.09	13.9	18.0	0.42
6CB-AuNPs	4.49×10^{-43}	3.03	6.33	6.01	11.5	29.6	0.36

material has a high ratio of excited-state to ground state absorption cross-section ($\delta_{exc}/\delta_0 \gg 1$), a long triplet lifetime with respect to pulse width, faster rate of intersystem crossing to triplet state ($\tau_T \gg \tau_{isc}$) and high triplet quantum yield.

Table 2 shows the absorption cross-sections resulting from the excited singlet, triplet and ground states. The NLO response resulting from the excited singlet (δ_1) was observed between 2.02×10^{-16} cm^2 and 6.33×10^{-16} cm^2 (7–22 times higher than δ_0). The corresponding triplet (δ_2) ranges from 3.97×10^{-16}–6.01×10^{-16} (13–30 times higher than δ_0). This is expected since at higher fluence and longer pulse durations, Pcs exhibit RSA in the visible spectrum resulting from the strong absorption from the singlet and/or triplet manifold. The absorption cross-sections reported in this work are in the same order of magnitude as those reported in the literature.[45,47–49] Yuksek and coworkers reported a high ratio of 20 between the excited state and ground state absorption cross-section in indium and gallium phthalocyanines studied using 4 ns laser pulses at 532 nm.[46] A ratio of about 13 for indium and thallium phthalocyanines was measured by Dini *et al.* using 7 ns at 532 nm[50] while Mendoca *et al.* reported a ratio of 9 using a 6 ns pulse at 532.[51] The simultaneous absorption of two photon with the same or different energy from the ground state to higher excited state results in two photon absorption depicted as TPA in Fig. 8. In the nanosecond regime, excited state induced TPA has been shown to be the dominant mechanism leading to additional nonlinear absorption in the nanosecond pulse duration.[52] The contribution to the RSA due to the TPA (δ_{TPA}) pathway ranges from 1.36×10^{-48}–4.49×10^{-43} cm^4 s photon^{-1}.

The AuNP conjugates produced a more significant TPA mechanism compared to AgNPs, probably due to the SPR absorption band of AuNPs at 530 nm, which is in complete resonance with the 532 nm wavelength employed in the Z-scan experiment.

To probe further into the nonlinear optical behaviour of the complexes in relation to change in intensities of the laser, the transmittance was plotted against input fluence, (Fig. S9, ESI†). It was observed that the transmittance exponentially decreases with increase in laser intensity (I_0), which is typical of reverse saturable absorbers.[39,53] One vital application of nonlinear optics is in optical limiting. The limiting threshold is an important term in optical limiting measurement and can be defined as the input fluence at which transmittance is 50% of the linear transmittance.[54] The display of reduced transmittance as a function of incident fluence is a prerequisite for an ideal optical material.

At a reduced incident fluence, the material exhibits linear transmittance; but abruptly changes to nonlinear transmittance as the incident light reaches the critical fluence or threshold, leading to clamping of the output fluence at a constant value

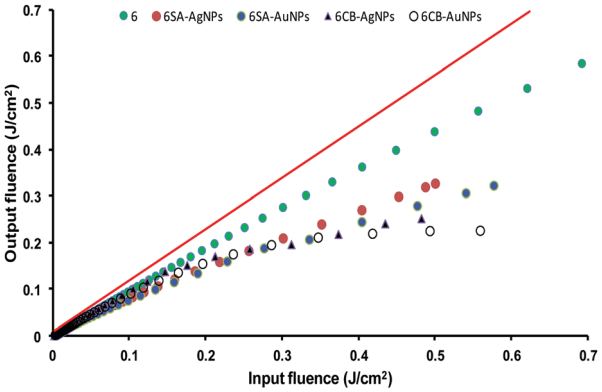

Fig. 11 Output (I_{out}) *vs.* Input (I_{in}) fluence of complex **6** and the nanoconjugates in DMSO.

that would presumably be less than the amount required to damage the optical element. The lower the I_{lim} value, the better the material as an optical limiter.

Fig. 11 shows the optical limiting curves obtained for **6** and its corresponding nanoconjugates. A nonlinear relationship was observed between fluence and transmittance with I_{lim} values of between 0.36 and 0.87 J cm^{-2} (Table 2). The nanoconjugates consistently exhibit stronger RSA and better optical limiting properties than **6**. The enhanced optical limiting behaviour of the nanoconjugates could be attributed to the presence of heavy atoms from the nanoparticles.

Conclusions

The optical limiting performance of 4-(2,4-bis(4-aminophenoxy)-phenoxy) phthalocyinato zinc(II) (**6**) and the corresponding surface assembled or covalently linked nanoconjugates with gold and silver nanoparticles has been investigated. A decrease in fluorescence quantum yields with corresponding increase in triplet and singlet oxygen quantum yield was observed for the nanoconjugates compared to complex **6** alone. The experimental open-aperture nanosecond Z-scan technique at 532 nm with 10 ns pulse duration was described using five model rate equations. The nonlinear optical response showed strong RSA behaviour for complex **6** alone and when conjugated to nanoparticles. It was found that complex **6** exhibits an enhanced nonlinear optical response when conjugated to nanoparticles.

Conflicts of interest

There are no conflicts to declare.

Acknowledgements

Technology (DST) and National Research Foundation (NRF) of South Africa through the DST/NRF South African Research Chairs Initiative for Professor of Medicinal Chemistry and Nanotechnology (UID 62620), and Rhodes University are acknowledged.

References

1 D. Dini, M. Barthel, T. Schneider, M. Ottmar, S. Verma and M. Hanack, *Solid State Ionics*, 2003, 289–330.
2 C. P. Singh, K. S. Bindra, B. Jain and S. M. Oak, *Opt. Commun.*, 2005, **245**, 407–414.
3 G. de la Torre, P. Vázquez, F. Agulló-López and T. Torres, *J. Mater. Chem.*, 1998, **8**, 1671–1683.
4 C. G. Claessens, W. J. Blau, M. Cook, M. Hanack, R. J. M. Nolte, T. Torres and D. Wöhrle, *Mol. Mater. Funct. Polym.*, 2001, 3–11.
5 E. M. García-Frutos, S. M. O'Flaherty, E. M. Maya, G. de la Torre, W. Blau, P. Vázquez and T. Torres, *J. Mater. Chem.*, 2003, **13**, 749–753.
6 I. Papagiannouli, P. Aloukos, D. Rioux, M. Meunier and S. Couris, *J. Phys. Chem. C*, 2015, **119**, 6861–6872.
7 S. Dengler, C. Kübel, A. Schwenke, G. Ritt and B. Eberle, *J. Opt.*, 2012, **14**, 075203.
8 N. Sreekumaran, A. V. Suryanarayanan, T. Pradeep, J. Thomas, M. Anija and R. Philip, *Mater. Sci. Eng., B*, 2005, **117**, 173–182.
9 O. M. Bankole and T. Nyokong, *J. Photochem. Photobiol., A*, 2016, **319–320**, 8–17.
10 O. M. Bankole, O. Osifeko and T. Nyokong, *J. Photochem. Photobiol., A*, 2016, **329**, 155–166.
11 N. Nwaji, B. Jones, J. Mack, D. O. Oluwole and T. Nyokong, *J. Photochem. Photobiol., A*, 2017, **346**, 46–59.
12 N. Rapulenyane, E. Antunes and T. Nyokong, *New J. Chem.*, 2013, **37**, 1216–1223.
13 N. Masilela and T. Nyokong, *J. Photochem. Photobiol., A*, 2011, **223**, 124–131.
14 H. Hiramatsu and F. E. Osterloh, *Chem. Mater.*, 2004, **16**, 2509–2511.
15 M. J. Frisch, G. W. Trucks, H. B. Schlegel, G. E. Scuseria, M. A. Robb, G. Cheeseman, J. R. Scalmani, V. Barone, B. Mennucci, H. Petersson, G. A. Nakatsuji, M. Caricato, X. Li, H. P. Hratchian, A. F. Izmaylov, J. Bloino, G. Zheng, J. L. Sonnenberg, K. Hada, M. Ehara, M. Toyota, R. Fukuda, J. Hasegawa, M. Ishida, T. Nakajima, Y. Honda, O. Kitao, H. Nakai, T. Vreven, J. A. Montgomery, Jr, J. E. Peralta, F. Ogliaro, M. Bearpark, J. J. Heyd, E. Brothers, K. N. Kudin, R. Staroverov, V. N. Kobayashi, K. Normand, J. Raghavachari, A. Rendell, J. C. Burant, S. S. Iyengar, J. Tomasi, M. Cossi, N. Rega, J. M. Millam, M. Klene, J. E. Knox, J. B. Cross, V. Bakken, C. Adamo, J. Jaramillo, R. Gomperts, R. E. Stratmann, O. Yazyev, A. J. Austin, R. Cammi, C. Pomelli, J. W. Ochterski, R. L. Martin, K. Morokuma, V. G. Zakrzewski, G. A. Voth, P. Salvador, S. Dannenberg, J. J. Dapprich, A. D. Daniels, Ö. Farkas, J. B. Foresman, J. V. Ortiz, J. Cioslowski and D. J. Fox, *Gaussian 09, Revision E. 01*, Gaussian, 2009.
16 R. J. Magyar and S. Tretiak, *J. Chem. Theory Comput.*, 2007, **3**, 976–987.
17 S. Fery-Forgues and D. Lavabre, *J. Chem. Educ.*, 1999, **76**, 1260–1264.
18 T. Nyokong and E. Antunnes, *Photochemical and photophysical properties of metallophthalocyanines: In the handbook of porphyrin science*, Academic Press, New York, 2010.
19 A. Ogunsipe, D. Maree and T. Nyokong, *J. Mol. Struct.*, 2003, **650**, 131–140.
20 N. Srinivasan, C. A. Haney, J. S. Lindsey, W. Zhang and B. T. Chait, *J. Porphyrins Phthalocyanines*, 1999, **32**, 283–291.
21 M. Gouterman, *Optical Spectra and Electronic Structure of Porphyrins and Related Rings*, ed. D. Dolphin, Academic Press, New York, 1978.
22 J. Mack and M. J. Stillman, *Coord. Chem. Rev.*, 2001, **219–221**, 993–1032.
23 J. Mack, N. Kobayashi and M. J. Stillman, *J. Inorg. Biochem.*, 2010, **102**, 472–479.
24 A. Kotiaho, R. Lahtinen, A. Efimov, H. K. Metsberg, E. Sariola, H. Lehtivuori, N. V. Tkachenko and H. Lemmetyinen, *J. Phys. Chem. C*, 2010, **114**, 162–168.
25 J. Hu and G. Jones, *J. Phys. Chem. B*, 1997, **104**, 11103–11109.
26 M. M. Alvarez, J. T. Khoury, T. G. Schaaf and M. N. Shafigullin, *J. Phys. Chem. B*, 2000, **101**, 3706–3712.
27 A. V. Zasedatelev, T. V. Dubinina, D. M. Krichevsky, V. I. Krasovskii, V. Y. Gak, V. E. Pushkarev, L. G. Tomilova and A. A. Chistyakov, *J. Phys. Chem. C*, 2016, **120**, 1816–1823.
28 Y. Noda, S. Noro1, T. Akutagawa and T. Nakamura, *Sci. Rep.*, 2014, **4**, 3758.
29 S. Thomas, S. K. Nair, E. A. Jamal, S. H. Al-Harthi, M. R. Varma and M. R. Anantharaman, *Nanotechnology*, 2008, **19**, 075710.
30 Y. Fleger and M. Rosenbluh, *Res. Lett. Opt.*, 2009, 4759415 pages.
31 E. Villarreal, G. G. Li, Q. Zhang, X. Fu and H. Wang, *Nano Lett.*, 2017, **17**, 4443–4452.
32 M. H. Majles Ara, Z. Dehghani, R. Sahraei, A. Daneshfar, Z. Javadi and F. Divsar, *J. Quant. Spectrosc. Radiat. Transfer*, 2012, **113**, 366–372.
33 R. Prabakaran, R. Kesavamoorthy, G. L. N. Reddy and F. P. Xavier, *Phys. Status Solidi*, 2002, **229**, 1175–1186.
34 R. Jenkins and R. L. Synder, *Introduction to X-ray diffractometry*, Wiley & Sons, New York, 1996.
35 S. J. Xiao, M. Textor and N. D. Spencer, *J. Mater. Sci.: Mater. Med.*, 1997, **8**, 867–872.
36 H. Zhang, S. D. Evans, J. R. Henderson, R. E. Miles and T. Shen, *J. Phys. Chem. B*, 2003, **107**, 6087–6095.
37 K. Sanusi, J. M. Stone and T. Nyokong, *New J. Chem.*, 2015, **39**, 1665–1677.
38 T. Nyokong, *Coord. Chem. Rev.*, 2007, **251**, 1707–1722.
39 K. L. Kelly, E. Coronado, L. L. Zhao and G. C. Schatz, *J. Phys. Chem. B*, 2003, **107**, 668–677.
40 H. I. Elim, J. Yang, J. Y. Lee, J. Mi and W. Ji, *Appl. Phys. Lett.*, 2006, **88**, 083107.

41 N. Venkatram, D. Narayana Rao, L. Giribabu and S. Venugopal Rao, *Chem. Phys. Lett.*, 2008, **464**, 211–215.
42 S. Venugopal Rao, P. T. Anusha, L. Giribabu and S. P. Tewari, *Pramana*, 2010, **75**, 1017–1023.
43 S. V. Rao, D. N. Rao, J. A. Akkara, B. S. DeCristofano and D. V. G. L. N. Rao, *Chem. Phys. Lett.*, 1998, **297**, 491–498.
44 T.-H. Wei, T.-H. Huang and T.-C. Wen, *Chem. Phys. Lett.*, 1999, **314**, 403–410.
45 C. Zhang, Y. Wang, J. Zhao, Q. Gary and G. M. Lawson, OSA Technical Digest (online) (Optical Society of America, 2015), paper NW4A.23.
46 M. Yüksek, A. Elmali, M. Durmuş, H. Gul Yaglioglu, H. Ünver and T. Nyokong, *J. Opt.*, 2010, **12**, 015208.
47 J. Zyss and D. S. Chemla, *Nonlinear Optical Properties of Organic Molecules and Crystals*, Academic Press, 1987, pp. 23–191.
48 M. G. Vivas, L. De Boni, L. Gaffo and C. R. Mendonca, *Dyes Pigm.*, 2014, **101**, 338–343.
49 M. G. Vivas, E. G. R. Fernandes, M. L. Rodríguez-Méndez and C. R. Mendonca, *Chem. Phys. Lett.*, 2012, **531**, 173–176.
50 D. Dini, J. F. Mario, M. Hanack, W. Chen and W. Ji, *ARKIVOC*, 2005, **2006**, 77–96.
51 C. R. Mendoca, L. Gaffo, L. Misoguti, W. C. Moreira, O. N. Oliveira and S. C. Zilio, *Chem. Phys. Lett.*, 2000, 300–304.
52 R. L. Sutherland, *Handbook of Nonlinear Optics*, Marcel Dekker, INC, New York, 2003, 2nd edn.
53 S. Hirata, K. Totani, T. Yamashita, C. Adachi and M. Vacha, *Nat. Mater.*, 2014, **13**, 938–946.
54 Y. Chen, L. Gao, M. Feng, L. Gu, N. He, J. Wang, Y. Araki, W. J. Blau and O. Ito, *Mini-Rev. Org. Chem.*, 2009, **6**, 55–65.